Finite Element Analysis Comparing the Formability of Large Hollow Protrusions in Tube Hydroforming

Vu Duc Quang
Faculty of Mechanical Engineering, University of Economics-Technology for Industries, No. 456 Minh Khai, Vinh Tuy Ward, Hanoi City, Vietnam
vuquang@uneti.edu.vn (corresponding author)

Received: 18 October 2025 | Revised: 26 November 2025 and 22 December 2025 | Accepted: 30 December 2025

 DOI: https://doi.org/10.48084/etasr.15637

ABSTRACT

The fabrication of large hollow protrusions for various types of metal joints using conventional stamping, welding, and casting methods often results in non-uniform deformation, material thinning, residual stresses, and thermal stresses. These issues compromise material continuity, reduce structural stiffness, and diminish overall strength. To address these challenges, the present study employs Tube Hydroforming (THF) technology to optimize the process of forming large hollow protrusions in T-shaped and X-shaped copper joints. The process was simulated using the Finite Element Method (FEM) in Abaqus/CAE 3DEXPERIENCE R2019, incorporating a plastic material model and nonlinear contact conditions to analyze and compare five critical parameters: the effective range of forming fluid pressure, the distribution of forming stress within the component, the components of plastic deformation, the wall thickness distribution, and the height of the large hollow protrusion. The results indicate that both joint types share the same effective forming fluid pressure range ($P_{i\text{-}max}$ = 23 MPa + 30 MPa), and the achieved height of a single protrusion is equivalent ($U1_{T(23\ MPa)}$ = 21.96 mm → $U1_{T(25\ MPa)}$ = 22.82 mm → $U1_{T(30\ MPa)}$ = 24.89 mm; $U1_{X(23\ MPa)}$ = 21.31 mm → $U1_{X(25MPa)}$ = 22.22 mm → $U1_{X(30MPa)}$ = 24.82 mm). Furthermore, the wall thinning at the apex of the large hollow protrusion was found to remain within acceptable limits for both components (thinning ratio: $\varepsilon_{min\text{-}T}$ = -24.17%, $\varepsilon_{min\text{-}X}$ = -10.83%), while the transition zone of the X-joint exhibited more intense thinning; yet remained within safe margins. This research provides a reliable three-dimensional simulation framework for optimizing the THF process, reducing experimental costs, and improving product quality in the manufacture of large hollow protrusions for various types of hollow joints.

Keywords-large hollow protrusion; T joint; X joint; THF; FEM

I. INTRODUCTION

THF is an advanced manufacturing process that employs high-pressure hydraulic fluid to form complex, lightweight, and structurally robust hollow components from tubular blanks [1]. This technology has significantly transformed component manufacturing in industries, such as automotive, aerospace, oil and gas, motorcycles and bicycles, and consumer electronics, by providing clear advantages over conventional metal-forming methods, including stamping, welding, and casting [2]. Compared with traditional processes, THF offers several key benefits, including weight reduction, improved structural integrity, part consolidation, efficient material utilization, greater design flexibility, and enhanced surface quality [3]. Owing to these advantages, THF is particularly well suited for producing components such as engine cradles, exhaust manifolds, and hollow joints, including T-shaped, X-shaped, and Y-shaped configurations [4].

Research has focused on optimizing THF processes through numerical simulations and experimental investigations. Authors in [5] emphasized the critical role of internal pressure and axial feeding in minimizing thinning ratios during the THF process. Their numerical and experimental results for copper tubes showed strong agreement-with a maximum deviation in branch height within ±5% and wall thickness within ±10% of the experimental values, thereby validating that finite element simulation can provide enhanced insights and improved control capabilities for the actual process. Authors in [6] employed an integrated Finite Element Simulation and Artificial Neural Network (FEM-ANN) approach to predict and optimize process parameters, namely counter force, axial displacement, and internal pressure, to address the multi-objective optimization problem in T-joint THF. They aimed to maximize the bulge ratio (H/D) while minimizing defects such as wall thinning and wrinkling. Authors in [7] successfully formed a complex T-shaped tubular part from GH4169 nickel-based superalloy at room temperature by developing a multi-step hydroforming process that incorporated intermediate annealing;

this methodology, supported by combined Finite Element Analysis (FEA) and physical experimentation on key parameters, including internal fluid pressure, axial feed, and counter pressure, effectively overcame the material's inherent ductility limitations to prevent failure. Authors in [8] developed a real-time, full-field simulation framework for THF by integrating FEM with a Machine Learning-based surrogate model, enabling instantaneous prediction of physical quantities like strain and wall thickness for rapid process monitoring and optimization. Authors in [9] classified stress states in THF into four groups and analyzed their distribution on the yield ellipse, emphasizing that balancing axial compression and internal pressure is critical to avoid defects such as wrinkling or bursting. Authors in [10] demonstrated that FEA can predict thinning and bulging behaviors with over 95% accuracy, reducing the need for physical testing and optimizing process parameters such as fluid pressure loading paths and axial feeds.

The integration of FEM simulations into THF processes has been transformative for design and optimization. FEM enables accurate prediction of formability parameters by modeling material behavior under complex loading conditions [11]. FEM-based numerical simulation software allows researchers to simulate loading paths and identify optimal parameters to prevent defects such as wrinkling or fracture [12]. Virtual prototyping through FEM reduces the need for physical trials, cutting development costs by 30%-40% and shortening production cycles. FEM facilitates the study of stress-strain states in critical regions, ensuring uniform deformation and structural integrity [13]. The present study aims to investigate the formation of large hollow protrusions in T and X joints using THF, focusing on five critical parameters: the effective forming fluid pressure range ($P_{i\text{-}Max}$), forming stress distribution, plastic strain components, wall thickness distribution, and the height of the large hollow protrusion. The novelty of this work lies in its comprehensive numerical-experimental approach, utilizing FEM simulations (Abaqus/CAE) to optimize the THF process for forming large, hollow protrusions in copper-based T and X joints [14]. By addressing the interplay between process parameters and formability outcomes, this research provides a framework for manufacturing high-quality hollow components with reduced costs and improved performance.

II. MATERIALS AND METHODS

A. Modeling and Meshing

The geometric models of the blank and forming dies, along with the material model, were established to closely match the practical conditions for the experimental implementation of the THF process to form large hollow protrusions on two types of hollow joints. A seamless copper tubular blank with an outer diameter D_0 = 22.22 mm, wall thickness t_0 = 1.2 mm, and length l_0 = 120 mm was modeled. Its geometric model (Figure 1(a)) and explicit mesh model (Figure 1(b)) were modeled as a deformable body with an elastic-plastic material definition. The tubular blank was meshed with 2340 elements. The element type was defined as Quad (S4R), utilizing a free meshing technique with a medial axis algorithm. The material model for the copper tubular blank, with its properties listed in Table I, was applied. The key dimensions for both the T-shaped and X-shaped hollow joint forming dies include a length of 130 mm, a width of 110 mm, and a thickness of 25 mm. The die cavity for housing the blank has a diameter equal to the blank's outer diameter (D_0). The die cavity for forming the large hollow protrusion has a diameter D_p = 25.04 mm, which is greater than D_0 (D_p > D_0 = 22.22 mm). The fillet radius in the die's transition region is Rf = 5 mm. The lower die, left punch, and right punch were modeled as discrete rigid bodies; the explicit mesh model of the die assembly is presented in Figure 2.

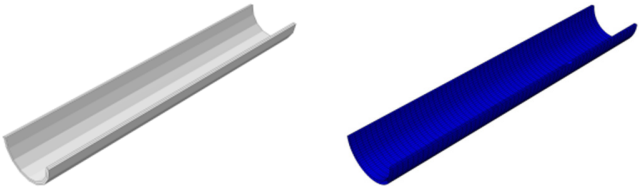

(a) (b)

Fig. 1. Models for the tubular blank: (a) geometric model, (b) finite element mesh model of the tubular blank.

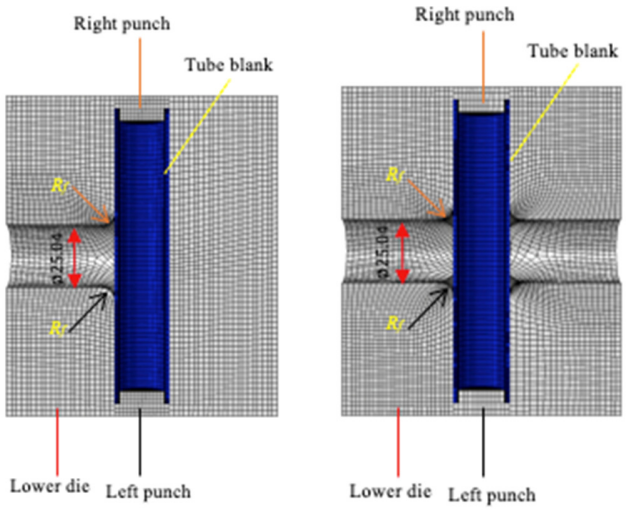

(a) (b)

Fig. 2. Die assembly and meshing.

TABLE I. MATERIAL PROPERTIES OF COPPER TUBE BLANK

Parameters	Value
Temperature (°C)	24
Density, ρ (kg/m^3)	8940
Young's modulus, E (Gpa)	115
Hardening coefficient, K (MPa)	325
Work hardening exponent, n	0.54
Poisson's ratio, v	0.33
Yield strength (MPa)	57.08
Ultimate tensile strength (MPa)	231.09
Elongation, ε_E (%)	42.75

B. Pressure Limits and Loading Paths

Identical boundary conditions were established for both THF process simulations using Abaqus/CAE 3DEXPERIENCE R2019 software. Each contacting surface

pair was assigned a penalty friction law with a coefficient of friction of μ = 0.1 [15]. The minimum internal fluid pressure (P_{min}) required to avoid wrinkling defects on the component during the forming of the large hollow protrusion can be estimated using [16]:

$$P_{min} = \left(0.13 + 1.15\frac{t_0}{D_p}\right)\sigma_Y \quad (1)$$

The maximum pressure (P_b) that can be applied without causing fracture at the large hollow protrusion apex can be calculated by [17]:

$$P_b = \sigma_U\left(\frac{4t_0}{D_p - t_0}\right) \quad (2)$$

where σ_Y = 57.08 MPa (yield strength), σ_U = 231.09 MPa (ultimate tensile strength), t_0 = 1.2 mm (initial wall thickness), and D_p = 25.04 mm (protrusion diameter). The calculated values are P_{min} = 7.83 MPa and P_b = 46.61 MPa. This pressure range provides an initial basis for determining the effective forming pressure window. The internal fluid pressure loading path (Amp-1) and the axial feed loading path/tube end (Amp-2) were defined according to the 20 s forming cycle detailed in Table II. The process parameters and output criteria of the 3D numerical simulations for the two THF processes were analyzed and specifically compared, as detailed below.

TABLE II. LOADING PATHS FOR THE TWO THF PROCESSES

Loading path - Amp-1			
Frequency	0	0.5	1
Amplitude	0	1	1
Loading path - Amp-2			
Frequency	0	0.5	1
Amplitude	0	1	1

III. RESULTS AND DISCUSSION

A. *Combination of Loading Paths in the Forming Process*

Figure 3 illustrates the combination of the forming fluid pressure range via loading path Amp-1 and the axial feed/tube end via loading path Amp-2, which enables effective forming of large hollow protrusions in both T and X components. Based on this effective forming pressure range for large hollow protrusions, four output parameters of the forming process were studied, analyzed, and compared.

When the $P_{i\text{-}max}$ pressure value exceeds this effective forming pressure range for large hollow protrusions, the forming stress may surpass the ultimate tensile strength (σ_U = 231.09 MPa), causing excessive biaxial stretching that leads to fracture at the large hollow protrusion apex during forming. At an increased pressure value of $P_{i\text{-}max}$ = 35 MPa, the T-shaped hollow component exhibited stresses reaching σ_U = 231.09 MPa throughout the entire transition zone and partially at the protrusion apex region at the 9th s, resulting in fracture at the large hollow protrusion apex at the 10th s, as shown in Figure 4(a). Similarly, the X-shaped hollow component showed stresses of σ_U = 231.09 MPa across nearly the entire transition zone and the expansion zone for large hollow protrusion formation at the 13th s, leading to fracture at the large hollow protrusion apex at the 14th s, as illustrated in Figure 4(b).

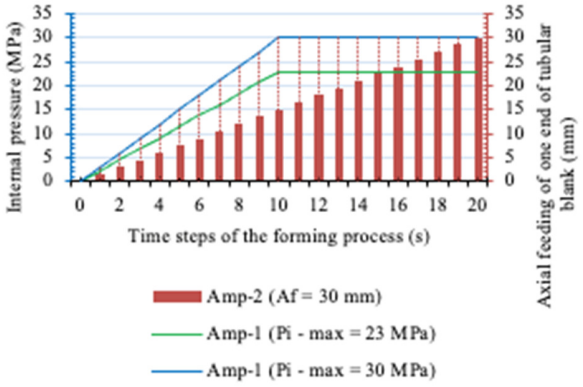

Fig. 3. A combination of the forming fluid pressure range via loading path Amp-1 and the axial feed/tube end via loading path Amp-2 ,enabling effective forming of large hollow protrusions in T and X components.

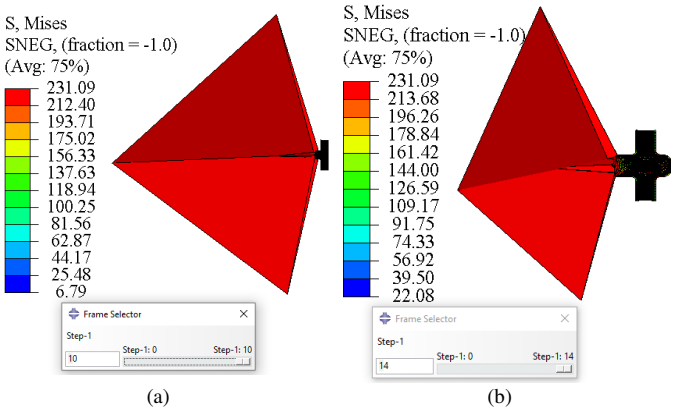

Fig. 4. Critical fluid pressure limit causing fracture at the large hollow protrusion apex, with process parameters $P_{i\text{-}max}$ = 35 MPa, Af = 30 mm: (a) T-joint, (b) X-joint.

B. *Von Mises Forming Stress Distribution*

The distribution of Von Mises forming stress (S) in the two hollow joints, with process parameters $P_{i\text{-}max}$ x = 30 MPa and Af = 30 mm, is depicted in Figure 5. In the T-joint, the entire guiding zone and transition zone reached the maximum stress value of S_{max} = 231.09 MPa. The expansion zone for large hollow protrusion formation exhibited relatively high stress values within the safe limit of 110.8 MPa-213.91 MPa. In the X-joint, the entire transition zone reached S_{max} = 231.09 MPa (due to high shear stress $S12$ from bending and significant friction with the die wall). The guiding zone and expansion zone for large hollow protrusion formation showed relatively high stress values within the safe limit of 105.53 MPa-213.16 MPa. Although the stress reached S_{max} = 231.09 MPa, it did not pose a danger to these regions because the tube wall was pressed firmly against the die cavity, enhancing the component's stiffness and strength through work hardening distinct advantage of the THF process.

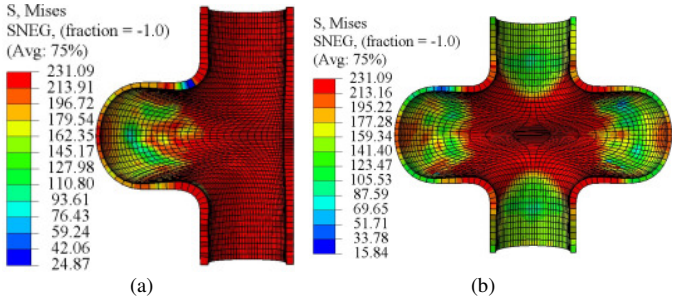

Fig. 5. Distribution of von Mises forming stress in the components with process parameters P_{i-max} = 30 MPa, Af = 30 mm: (a) T-joint, (b) X-joint.

C. Plastic Strain

Figure 6 illustrates the distribution of plastic strain (PE) components in the two components formed under identical process parameters, P_{i-max} = 30 MPa and Af = 30 mm. In the guiding zone of both components, the PE values are negative due to the axial compressive stress S33, which promotes material feeding from both tube ends. Specifically, the minimum plastic strain values are PE_{min}-T = −0.21 for the T-joint and PE_{min}-X = −0.08 for the X-joint. Owing to the presence of two large hollow protrusions symmetrically arranged about the tube axis, the X-joint exhibits a more symmetric and balanced PE distribution compared with the T-joint, which contains only a single protrusion. The transition zones of the two components exhibit different PE distributions along both the axial direction and the direction perpendicular to the tube axis. In the T-joint, the axial material flow region experiences compressive deformation, with PET ranging from −0.21 to −0.02, whereas the region with material flow perpendicular to the tube axis shows tensile–shear deformation, with PET ranging from 0.17 to 0.93. This behavior is primarily attributed to shear stress S12 and frictional interaction with the die wall, with deformation initiating at the center of the expanding blank and propagating toward the forming large hollow protrusion.

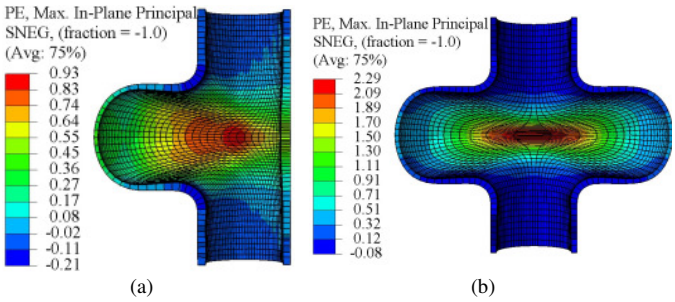

Fig. 6. Distribution of plastic strain components in the components with process parameters P_{i-max} = 30 MPa, Af = 30 mm: (a) T-joint, (b) X-joint.

The values of PE_{max} in both components across the effective forming pressure range are presented in the chart in Figure 7, and are consistent with [5]. A rise in P_{i-max} leads to a steeper increase in PE_{max}-X for the X-joint relative to the increase in PE_{max}-T for the T-joint. The difference in ΔPE_{max} between the two components also gradually increases with higher P_{i-max}. At P_{i-max} = 23 MPa, ΔPE_{max} (23 MPa) = PE_{max}-X (23 MPa) - PE_{max}-T (23 MPa) = 2.14 - 0.77 = 1.37; at P_{i-max} = 25 MPa, ΔPE_{max} (25 MPa) = PE_{max}-X (25 MPa) - PE_{max}-T (25 MPa)) = 2.18 - 0.8 = 1.38; and at P_{i-max} = 30 MPa, ΔPE_{max} (30 MPa) = PE_{max}-X (30 MPa) - PE_{max}-T (30 MPa) = 2.29 - 0.82 = 1.47. PE_{max}-X = 2.29 approaches the ductility limit (ε_E = 42.75%) but remains safe due to die contact constraint.

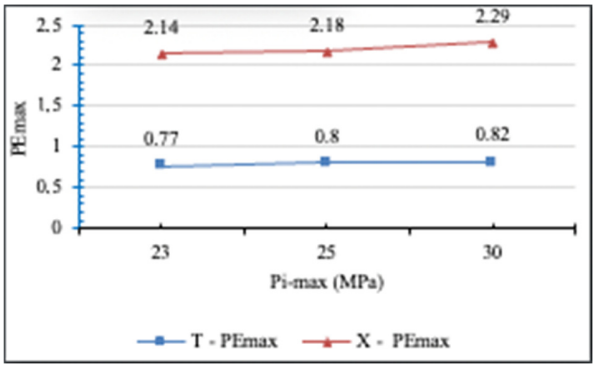

Fig. 7. Comparison of PE_{max} in the components across the effective forming fluid pressure range for large hollow protrusions.

D. Wall Thickness Distribution

The wall thickness (STH) distribution in the two components with process parameters $P_{i\text{-max}}$ = 30 MPa and Af = 30 mm is illustrated in Figure 8. The guiding zone in the T-joint exhibits more severe thickening compared to the X-joint, specifically STHT = 1.76 mm to 2 mm (thickening ratio = 46.67% to 66.67%) versus STHX = 1.35 mm to 1.63 mm (thickening ratio = 12.5% to 35.83%). The transition zone exhibits distinctly different wall thickness distributions in the two components. In the T-joint, the tube wall undergoes relatively uniform thickening throughout this region, reaching a maximum thickness of $STH_{max\text{-}T}$ = 2.36 mm (corresponding to 96.67% thickening) at the tube wall section located opposite the large hollow protrusion relative to the tube center. In contrast, the X-joint experiences a combination of wall thinning and thickening within the transition zone. From the tube center toward the two large hollow protrusions, the wall undergoes pronounced thinning due to the high tensile stress component S11, reaching a minimum thickness of $STH_{min\text{-}X}$ = 0.69 mm (–42.5% thinning). Despite this severe thinning, structural safety and stiffness are maintained because the tube wall remains in continuous contact with the die cavity during plastic deformation (Figure 8(d)). Conversely, along the axial direction in the filleted region with radius Rf, material accumulation leads to wall thickening, with the thickness increasing to a maximum value of $STH_{max\text{-}X}$ = 1.81 mm (50.83% thickening).

The expansion zones of both components exhibit similar deformation behavior, characterized by slight wall thickening in regions where the tube wall remains in contact with the die cavity, while wall thinning is confined primarily to the spherical crown of the large hollow protrusion. The minimum values are $STH_{min\text{-}T}$ = 0.91 mm (thinning ratio $\varepsilon_{min\text{-}T}$ = -24.17%) (Figures 8(a) and 8(c)) and $STH_{min\text{-}X}$ = 1.07 mm (thinning ratio $\varepsilon_{min\text{-}X}$ = -10.83%) (Figures 8(b) and 8(d)). The thinning ratios at the spherical crowns of both components meet the required

criteria as they exceed the allowable limit of ε_{min} = -30% (corresponding to STH_{min} = 0.84 mm) for copper material. The STH_{min} values in both components across the effective forming pressure range for large hollow protrusions are compared with each other and with the initial blank thickness t_0 in Figure 9. Increasing $P_{i\text{-}max}$ reduces STH_{min} (while ensuring it remains greater than STH_{min} = 0.84 mm). However, there is a difference in the location of the STH_{min} distribution. In the T-joint, $STH_{min\text{-}T}$ is located at the spherical crown of the expansion zone, forming the large hollow protrusion: t_0 = 1.2 mm → 1 mm ($P_{i\text{-}max}$ = 23 MPa) → 1.01 mm ($P_{i\text{-}max}$ = 25 MPa) → 0.91 mm ($P_{i\text{-}max}$ x = 30 MPa). In contrast, $STH_{min\text{-}X}$ is located in the transition zone from the tube center (tube wall contacting the die wall), expanding toward the two large hollow protrusions: t_0 = 1.2 mm → 0.8 mm ($P_{i\text{-}max}$ = 23 MPa) → 0.77 mm ($P_{i\text{-}max}$ = 25 MPa) → 0.68 mm ($P_{i\text{-}max}$ = 30 MPa).

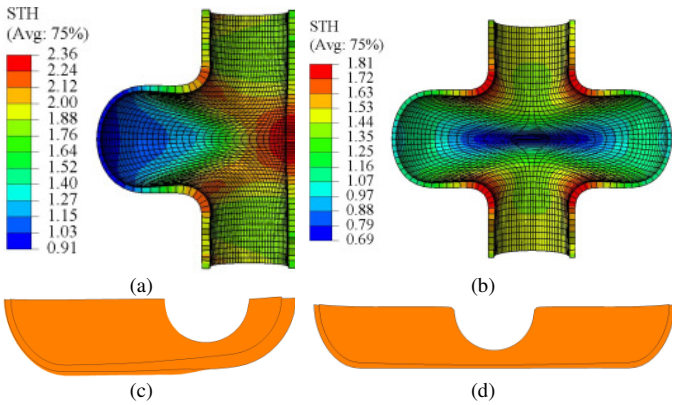

Fig. 8. Wall thickness distribution in the components with process parameters $P_{i\text{-}max}$ = 30 MPa, Af = 30 mm: section of T-joint: (a) cross-section containing the tube axis and (c) cross-section perpendicular to the T-joint tube axis; section of X-joint: (b) cross-section containing the tube axis and (d) cross-section perpendicular to the X-joint tube axis.

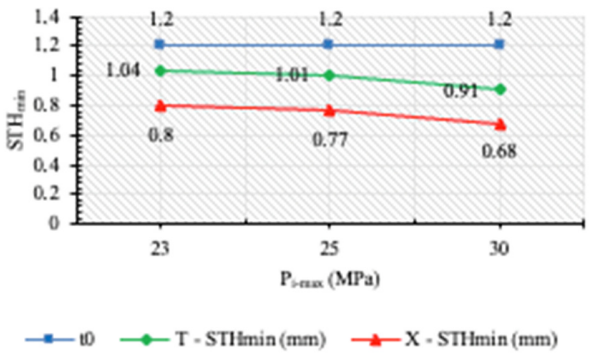

Fig. 9. Comparison of STHmin in the components across the effective forming fluid pressure range for large hollow protrusions.

E. Height of Single and Double Large Hollow Protrusions

The height of the large hollow protrusion (U1) in both components formed with the same process parameters, $P_{i\text{-}max}$ = 30 MPa and Af = 30 mm, is shown in Figure 10. The T and X joints achieve equivalent single protrusion heights, both exceeding the initial blank diameter: $U1T = |-24.89|$ mm ≈ $U1_X$ = 24.82 mm > D_0 = 22.22 mm. The formation of two large hollow protrusions in the X-joint achieves a total height of 2U1X = 49.64 mm, double the height of the single protrusion formed in the T-joint. The protrusion heights U1 and 2U1 of both components across the effective forming pressure range for large hollow protrusions, with a total axial feed Af_Σ = 60 mm, are compared in Figure 11. The results show that increasing $P_{i\text{-}max}$ increases U1 of the single large hollow protrusion. Specifically, for the T-joint (U1T shown in red bars on the chart): $U1_{T\ (23\ MPa)}$ = 21.96 mm → $U1_{T\ (25\ MPa)}$ = 22.82 mm → $U1_{T\ (30\ MPa)}$ = 24.89 mm. For the X-joint (U1X shown in green bars): $U1_{X\ (23\ MPa)}$ = 21.31 mm → $U1_{X\ (25\ MPa)}$ = 22.22 mm → $U1_{X\ (30\ MPa)}$ = 24.82 mm. At each $P_{i\text{-}max}$ value within the effective forming pressure range, the height of a single large hollow protrusion achieved in both components is quite similar. However, the total height of the two large hollow protrusions formed in the X-joint (2U1X shown in blue bars on the chart): $2U1_{X(23\ MPa)}$ = 42.62 mm → $2U1_{X(25\ MPa)}$ = 44.44 mm → $2U1_{X(30\ MPa)}$ = 49.64 mm demonstrates higher efficiency compared to the protrusion height formed in the T-joint when using the same total axial feed Af_Σ = 60 mm (shown in orange bars on the chart).

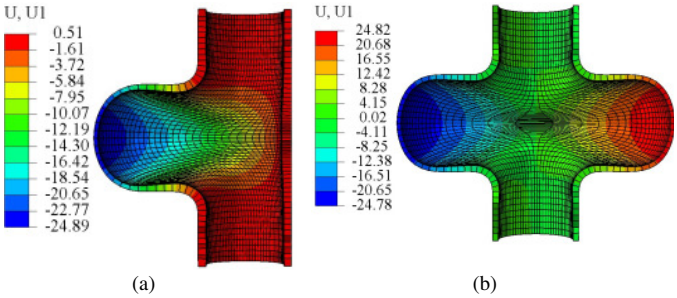

Fig. 10. Height of the large hollow protrusion in the components with process parameters $P_{i\text{-}max}$ = 30 MPa, Af = 30 mm: (a) T-joint, (b) X-joint.

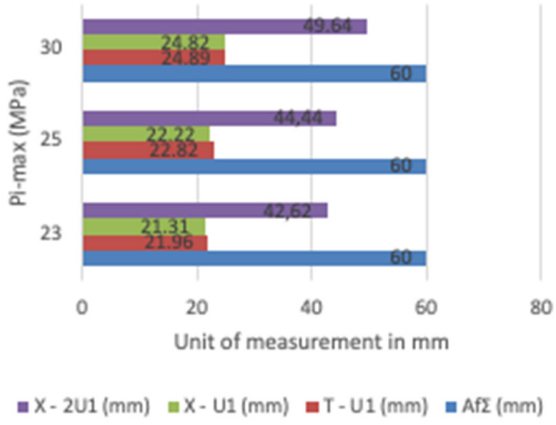

Fig. 11. Comparison of U1 in the components across the effective forming fluid pressure range for large hollow protrusions.

IV. CONCLUSIONS

Unlike previous studies that focused on copper T- or X-joints in isolation, this work directly compares their formability by systematically evaluating five key criteria via finite element

simulation. The key findings include the identification of an effective forming fluid pressure range ($P_{i\text{-}max}$ = 23 MPa to 30 MPa) and axial feed parameters (Af = 30 mm per tube end), which prevent cracking while ensuring satisfactory outcomes for all four output criteria. The forming stress in the large hollow protrusion apex region of both components remains safe and below σ_U. Although the guiding and transition zones reach σ_U, the structural integrity is maintained due to continuous tube-die contact. The plastic strain (PE) components distributed in the T-joint are smaller and safer compared to those in the X-joint. The T-joint demonstrates superior formability, characterized by reduced wall thinning. The minimum thickness ($STH_{min\text{-}T}$ = 0.91 mm), which corresponds to a thinning strain of $\varepsilon_{min\text{-}T}$ = -24.17%, occurs specifically at the apex of the large hollow protrusion in the expansion zone.

In contrast to the T-joint, the X-joint exhibits its most severe wall thinning in the transition zone between the tube center and the two large hollow protrusions. This results in a substantially reduced minimum wall thickness of $STH_{min\text{-}X}$ = 0.68 mm, corresponding to a thinning strain of $\varepsilon_{min\text{-}X} = -42.5\%$. Nevertheless, the thinned region remains technically safe due to continuous contact between the tube wall and the die cavity during plastic deformation, as well as the strengthening effect induced by work hardening. Although the height of a single large hollow protrusion (U1) is nearly identical in both components, the X-joint demonstrates superior formability in terms of the total protrusion height (2U1), owing to the formation of two symmetric protrusions. Overall, these findings provide a reliable basis for die design and process parameter optimization in Tube Hydroforming (THF) of large hollow protrusions for both experimental investigations and industrial applications.

REFERENCES

[1] Harjinder Singh, Fundamentals of Hydroforming. The Society of Manufacturing Engineers, 2003.

[2] S. Chinchanikar, H. Mulik, P. Varude, S. Atole, and N. Mundada, "A review of emerging hydroforming technologies: design considerations, parametric studies, and recent innovations," *Journal of Engineering and Applied Science*, vol. 71, no. 1, Oct. 2024, Art. no. 205, https://doi.org/10.1186/s44147-024-00546-z.

[3] C. Bell, J. Corney, N. Zuelli, and D. Savings, "A state of the art review of hydroforming technology," *International Journal of Material Forming*, vol. 13, no. 5, pp. 789–828, Sept. 2020, https://doi.org/10.1007/s12289-019-01507-1.

[4] N. V. Pham, Hydraulic Stamping Technology. Hanoi University of Science and Technology, 2006.

[5] P. Ray and B. J. Mac Donald, "Experimental study and finite element analysis of simple X- and T-branch tube hydroforming processes," *International Journal of Mechanical Sciences*, vol. 47, no. 10, pp. 1498–1518, Oct. 2005, https://doi.org/10.1016/j.ijmecsci.2005.06.007.

[6] F. Abbassi, F. Ahmad, S. Gulzar, T. Belhadj, A. Karrech, and H. S. Choi, "Design of T-shaped tube hydroforming using finite element and artificial neural network modeling," *Journal of Mechanical Science and Technology*, vol. 34, no. 3, pp. 1129–1138, Mar. 2020, https://doi.org/10.1007/s12206-020-0214-4.

[7] X.-L. Cui, B. Teng, and S. Yuan, "Hydroforming process of complex T-shaped tubular parts of nickel-based superalloy," *CIRP Journal of Manufacturing Science and Technology*, vol. 32, pp. 476–490, Jan. 2021, https://doi.org/10.1016/j.cirpj.2021.02.001.

[8] L. Cheng, H. Guo, L. Sun, C. Yang, F. Sun, and J. Li, "Real-Time Simulation of Tube Hydroforming by Integrating Finite-Element Method and Machine Learning," *Journal of Manufacturing and Materials Processing*, vol. 8, no. 4, Aug. 2024, Art. no. 175, https://doi.org/10.3390/jmmp8040175.

[9] H. Y. Li, X. S. Wang, S. J. Yuan, Q. B. Miao, and Z. R. Wang, "Typical stress states of tube hydroforming and their distribution on the yield ellipse," *Journal of Materials Processing Technology*, vol. 151, no. 1, pp. 345–349, Sept. 2004, https://doi.org/10.1016/j.jmatprotec.2004.04.085.

[10] B. G. Marlapalle and R. S. Hingole, "Predictions of formability parameters in tube hydroforming process," *SN Applied Sciences*, vol. 3, no. 6, May 2021, Art. no. 606. https://doi.org/10.1007/s42452-021-04533-4.

[11] Y.-M. Hwang, Y.-J. Wang, C.-C. Chen, and H.-S. R. Tsui, "Performance evaluation and loading path design in tube hydroforming of multi-convolution metal bellows," *The International Journal of Advanced Manufacturing Technology*, vol. 141, no. 5, pp. 3241–3258, Nov. 2025, https://doi.org/10.1007/s00170-025-16611-7.

[12] S. Jirathearanat, "Advanced methods for finite element simulation for part and process design in tube hydroforming," M.S. Thesis, The Ohio State University ProQuest, USA, 2004.

[13] N. D. Trung and V. D. Quang, "The Influence of the Protrusion Inclination Angle on the Formability of Hollow Joint in the Tube Hydroforming Process," *Journal of Machine Engineering*, pp. 83–96, Oct. 2025, https://doi.org/10.36897/jme/203468.

[14] D. Berry, "R2019x Release: Established Products," *Dassault Systèmes blog*, Dec. 13, 2018. https://blog.3ds.com/brands/simulia/r2019x-release-established-products/.

[15] R. Neugebauer, Ed., *Hydro-Umformung*. Springer Berlin Heidelberg, 2007.

[16] M. Koç, Hydroforming for Advanced Manufacturing. Elsevier, 2008.

[17] S. Jirathearanat, C. Hartl, and T. Altan, "Hydroforming of Y-shapes—product and process design using FEA simulation and experiments," *Journal of Materials Processing Technology*, vol. 146, no. 1, pp. 124–129, Feb. 2004, https://doi.org/10.1016/S0924-0136(03)00852-5.